Ultrasonics 153 (2025) 107658

Contents lists available at ScienceDirect

Ultrasonics

journal homepage: www.elsevier.com/locate/ultras

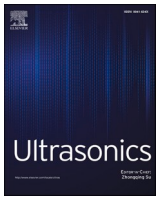

A procedure for simulation-assisted identification of ultrasonic wave attenuation in heterogeneous materials and its application to the detection of fracture in concrete beams

Erwin Wojtczak *, Magdalena Rucka

Department of Mechanics of Materials and Structures, Faculty of Civil and Environmental Engineering, Gdańsk University of Technology, Narutowicza 11/12, 80-233 Gdańsk, Poland

ARTICLE INFO

Keywords:
Concrete
Attenuation
Ultrasonic waves
Cumulative energy
Fracture monitoring

ABSTRACT

In this study, a novel procedure for identification of ultrasonic wave attenuation in heterogeneous materials based on signal energy was presented. The main objective was to develop a method for simple and robust determination of wave characteristics for further use in numerical modelling of ultrasonic wave propagation including attenuation of signals. Experimental investigations supported by numerical simulations were proposed as an approach to determine the mass proportionality coefficient in the Rayleigh proportional damping model. A number of concrete samples with different sensor configurations were investigated to prove the efficiency of the developed algorithm. The limitations of the established approach were characterized, specifically the maximum frequency that can be considered should be determined in advance. The ability of the proposed method to detect fracture in concrete samples under three-point bending was initially verified for further development of the attenuation-based diagnostic technique.

1. Introduction

Concrete structures are among the most widely used in civil engineering today because of their high load-bearing capacity, durability, and relatively low production costs. Despite their many advantages, there are some significant issues that need to be addressed. First of all, concrete is a brittle material that tends to crack during service. The appearance of small cracks induced by shrinkage or exceeding of strength in tension areas is a common phenomenon in properly designed and manufactured concrete. However, if the cracks propagate and dilate excessively, there is a risk of catastrophic failure due to fracture of concrete itself or rebar corrosion resulting from the penetration of water or chemical aggression. This issue leads to an increasing interest in the diagnostics of concrete structures, preferably using non-destructive techniques.

Due to its high reliability and wide range of applications, the phenomenon of elastic wave propagation is the basis of numerous methods dedicated to the non-invasive monitoring of state of structural elements [1–6]. The waves are excited using an external source (e.g., ultrasonic transducer) on the surface of tested element (active sensing) or can arise as a result of changes in the structure of the sample, e.g., cracking under load (passive approach). In the current study, the first approach is discussed. The excited waves can propagate in elastic medium and interact with its structural and material discontinuities, making them a significant tool for detecting and imaging of damage in various materials. One of the most important features of ultrasonic waves is their attenuation, i.e., the loss of intensity of signal amplitude during propagation, measured in different locations of the structure. Due to the high sensitivity to changes in the mechanical parameters of the medium and its internal structure, attenuation can provide a significant information about the current state of tested elements. In the case of heterogeneous materials, such as concrete, attenuation can be used to characterise the aggregate distribution, the concrete mix content or the presence of air voids.

Many researchers have used attenuation to characterise the mechanical performance and structure of cementitious elements. Gaydecki et al. [7] identified attenuation in concrete cylinders manufactured from various mixes (with different aggregate sizes). They determined the attenuation coefficient based on ultrasonic measurements performed with transducers differing in central frequencies to develop relations between attenuation coefficient and frequency. Berthelot et al. [8] investigated the influence of concrete composition, wave frequency and

* Corresponding author.
E-mail addresses: erwin.wojtczak@pg.edu.pl (E. Wojtczak), magdalena.rucka@pg.edu.pl (M. Rucka).

https://doi.org/10.1016/j.ultras.2025.107658
Received 9 January 2025; Received in revised form 10 March 2025; Accepted 4 April 2025
Available online 5 April 2025

propagation distance on the attenuation of different mortars and concretes. They tested rod-shaped samples with piezoelectric transducers attached to opposite ends of the rods and developed functions of the attenuation coefficient in relation to above mentioned factors. Philippidis and Aggelis [9] analysed the wave propagation phenomenon in different cementitious materials (mortar, paste and concrete). They experimentally investigated cubic samples using the through-transmission technique in order to determine the influence of the water to cement ratio on the attenuation-frequency relations. Abdullah and Sichani [10] tested cubic samples made of concrete and plaster. They observed a significant impact of different factors, namely, the water to cement ratio, type of cement, granulation of aggregates, and replacement of cement with micro-silica, on the attenuation coefficient.

Ultrasonic wave attenuation has also been used as an indicator of the presence of damage in concrete structures. Yim et al. [11] used attenuation for non-destructive evaluation of air voids in concrete and cement paste. They proposed inserting PZT material between the tested sample and the conventional ultrasonic transducer, and to self-compensate the recorded signals. A significant growth of attenuation with the increasing content of voids was observed, especially for higher wave frequencies. Sun and Zhu [12] considered damage identification in reinforced-concrete elements. They evaluated the attenuation of bare bars to determine the damping coefficients of high order ultrasonic wave modes and then tested three bars embedded in concrete (one without defect, and two damaged, with honeycomb insert and void). Attenuation was found to be effective in detecting internal defects early in the curing process as well as at later stages.

An important aspect of ultrasonic wave-based non-destructive testing is the modelling of the wave propagation phenomenon. Numerical simulations can be a significant tool supporting the interpretation and evaluation of experimental results. There are a number of approaches to modelling wave attenuation from which one of the simplest and most commonly used being Rayleigh proportional damping [13,14]. It consists of determining the mass and stiffness proportionality coefficients to determine the damping matrix. Ramadas et al. [14] considered the modelling of ultrasonic wave attenuation in glass/epoxy laminates using the influence of both coefficients. They compared numerical simulations in finite element models with experimental results, obtaining a good agreement between the two approaches. Tian et al. [15] investigated the ultrasonic wave attenuation of stress waves in concrete beams. They developed an absorption attenuation model based on Rayleigh damping theory and time-reversal method. The predicted attenuation coefficients were verified by related experimental measurements. Mohseni and Ng [16] detected debonding between fibre-reinforced polymer and concrete samples. They prepared 3D numerical models in Abaqus using Rayleigh damping and verified the results obtained with experimental investigations. Treiber et al. [17] analysed the influence of sand aggregate (different volume fractions) on the attenuation of concrete. They predicted the values of the attenuation coefficient using numerical models and compared the results with experimental investigations, obtaining a good agreement of both approaches. Sepehrinezhad and Toufigh [18] considered damage identification in polymer concrete samples. They tested concrete prisms prepared from different concrete mixes using various wave frequencies. The authors proved that attenuation was effective in evaluating micro-defects at an early stage of mechanical degradation. Additionally, they performed a model prediction of the wave signals and compared them with experimental results, obtaining satisfactory agreement. Ramaniraka et al. [19] determined the contribution of absorption and multiple scattering to the attenuation of elastic waves propagating in concrete samples. They investigated the influence of the contact level between aggregate and mortar in order to improve the agreement between numerical and experimental results. Yu et al. [20] built a 2D numerical model of concrete beams using the spectral element method. They considered wave attenuation and phase velocity measurements as leading factors in the calibration of the model. A significant conclusion of the analysis was that the aggregate orientation had a significant effect on the wave parameters obtained. In recent years, some works utilizing machine learning and neural networks have been reported for the prediction and identification of attenuation in seal coatings [21], tissue mimicking media [22–24], polyethylene pipes [25], and origami structures [26].The above-described works dealt with the identification of attenuation using classical approach, i.e., based on the amplitudes of signals collected in different sensors. It should be noted that this approach can be problematic while considering the experimental challenges with coupling conditions between the sensors and the sample surface, which can lead to difficulties in the assessment of the amplitude of the received signals. Furthermore, the identification of the Rayleigh proportionality coefficients requires the value of the wave velocity, which leads to problems with the automated identification of the time of flight of the wave between sensors in the case of a large number of signals.

In the present work, a novel three-stage procedure for the identification of attenuation-related characteristics in concrete elements based on wave signal energy has been developed. The first stage requires numerical simulation of wave propagation in a simplified two-phase model of the analysed heterogeneous material for arbitrary assumed training datasets with different frequencies and mass proportionality coefficients α used in the Rayleigh proportional damping model. The second stage consists of experimental measurements of wave signals on the physical model and determination of experimental values of α. In the third stage, the evaluated α values are treated as testing dataset which is verified by additional numerical simulations. The results obtained from the investigations performed on concrete samples proved the efficiency of the procedure. The proposed algorithm eliminates the issue of inaccurate bonding of sensors to the sample surface, because, even in the case of weakened adhesion between a particular sensor and the sample surface, the energy changes are not affected. Furthermore, the method does not require the calculation of the wave velocity for each individual signal. The additional objective of the study was to verify whether the developed procedure could be used for the fracture characterisation in concrete beams under bending. It was essential to confirm that the mass proportionality coefficient in Rayleigh damping model determined using the currently developed algorithm is sensitive to cracking of concrete elements. However, it was only an initial step for further more advanced analysis dedicated to the development of the attenuation-based diagnostic algorithm.

2. Theoretical background of ultrasonic wave attenuation

In the dynamic analysis, a common model that allows wave attenuation to be included is Rayleigh proportional damping, which introduces damping into the equation of motion, resulting in a reduction of vibrations over time. In the case of ultrasonic waves (which are high-frequency vibrations), this leads to wave attenuation, i.e., loss of amplitude of the wave signals during propagation. The model assumes that the damping constant c is a linear combination of mass m and stiffness k [14,27]:

$$c = \alpha m + \beta k \tag{1}$$

In the above equation, α and β are the mass and stiffness proportionality coefficients, respectively. The coefficients are related to the damping ratio with respect to the formula:

$$\zeta = \frac{1}{2}\left(\frac{\alpha}{\omega} + \beta\omega\right) \tag{2}$$

The above described model can be simplified by eliminating one of the coefficients (α or β) [14]. While considering only mass damping, the above equation can be simplified by eliminating β, thus, the mass proportional factor can be calculated as:

$$\alpha = 2\omega\zeta \tag{3}$$

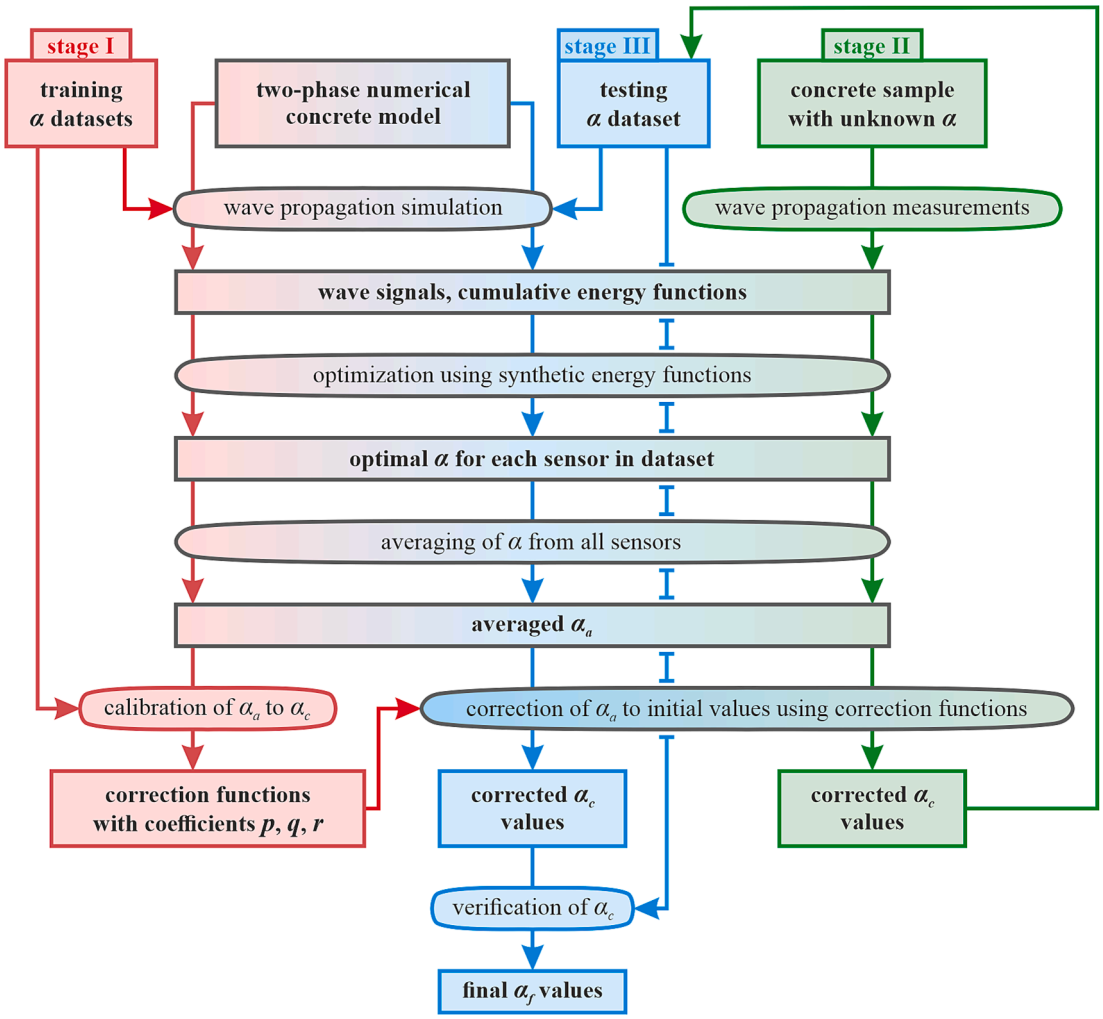

Fig. 1. Scheme for the determination of attenuation.

The elimination of any coefficient simplifies the problem, but in general can lead to an underestimation or overestimation of damping of the analysed structure. However, in the case of ultrasonic guided waves, some works have been carried out confirming the efficiency of using both coefficients and each of them separately (e.g., [14]).

For simple structural elements made of materials meeting the conditions of the homogeneous isotropic material model (such as steel bars – see [27]), in which the wave propagation is not disturbed by the internal structure, it is relatively easy to determine attenuation-related characteristics (damping ratios and proportionality coefficients) by analysing specific wave signals. In the case of heterogeneous materials, such as concrete, the analysis is more complex due to multiple reflections of ultrasonic waves at the aggregates. The influence of the concrete micro-structure depends on the wave frequency [28]. In a low frequency-range (modal analysis range, up to 20 kHz), particular grains do not significantly influence the propagating waves. Above this limit (ultrasonic range), there is simple scattering (up to about 150 kHz) and multiple scattering (diffusion, 150 kHz – 5 MHz) due to the interaction of waves with particular grains. These effects cause the wave signals to be less clear for interpretation. Therefore, a different approach has to be developed. In the current paper it is proposed to use the energy of the ultrasonic signals as an indicator of attenuation changes.

Let consider a continuous time-domain signal $s(t)$ determined between 0 and t_e. The total signal energy can be formulated as follows:

$$E_t = \int_0^{t_e} |s(t)|^2 \mathrm{d}t \tag{4}$$

The signal energy can be calculated for each specific time instance τ, creating a function of cumulative energy as a function of time:

$$E(\tau) = \int_0^{\tau} |s(t)|^2 \mathrm{d}t, \quad \tau \in \langle 0, t_e \rangle \tag{5}$$

In the case of discrete signals s_u with N samples, the cumulative energy function can be calculated numerically as:

$$E_T = \sum_{u=1}^{T} s_u^2, \quad T = 1, 2, \ldots, N \tag{6}$$

In certain cases, when the signal is expressed by an explicit function, the signal energy can be calculated analytically. For example, let consider a theoretical wave signal $s_c(t)$ in the form of a cosine function with the initial amplitude A, angular frequency ω, exponentially damped with a mass proportionality coefficient α, determined between 0 and t_e:

$$s_c(t) = A\cos(\omega t)e^{-\zeta\omega t} = A\cos(\omega t)e^{-\frac{\alpha t}{2}}, \quad t \in \langle 0, t_e \rangle \tag{7}$$

In this specific case, the cumulative signal energy can be computed as:

$$E(\tau) = \frac{A^2 e^{-\alpha\tau}}{2\alpha(\alpha^2 + 4\omega^2)} \cdot (4\omega^2(e^{\alpha\tau} - 1) + 2\alpha\omega \sin(2\tau\omega) - \alpha^2(1 + \cos(2\tau\omega) - 2e^{\alpha\tau})), \quad \tau \in \langle 0, t_e \rangle \tag{8}$$

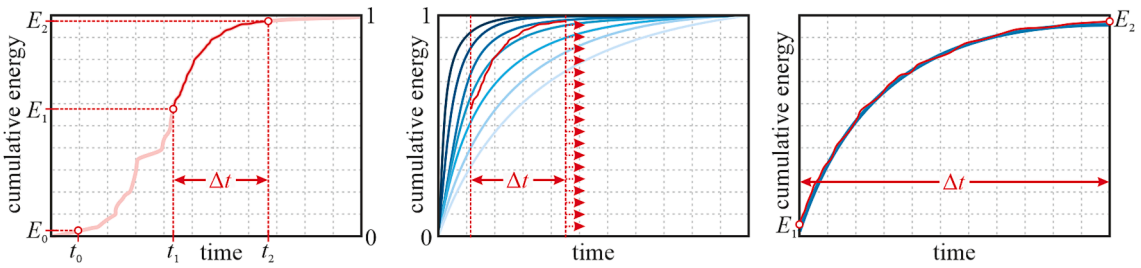

Fig. 2. Optimisation algorithm for determination of mass proportionality coefficient: a) cumulative energy of signal with established range for calculation; b) shortened signal energy function with synthetic cumulative energy functions for different mass proportionality coefficients; c) shortened signal energy function with fitted synthetic energy function.

It is evident that the cumulative energy depends on the angular frequency and the mass proportionality coefficient, and therefore the wave attenuation can be determined from the cumulative energy function. The typical ultrasonic wave signals recorded in concrete samples from the excitation in the form of a wave packet cannot be adequately described by a single cosine function. However, the apparently chaotic wave signals, resulting from the heterogeneous structure of material, are similar to the exponentially damped cosine, neglecting the initial part of the signal which is the result of a direct impact of the excitation.

3. A novel algorithm for signal energy-based identification of wave attenuation

In the current study, a novel algorithm for the identification of attenuation-related characteristics in concrete samples is presented (Fig. 1). First (stage I), training datasets are created with m different values of excitation frequency f_i and mass proportionality coefficients $\alpha_i^{(n)}$, $i = 1,2,\ldots,m$. In the current study two datasets were assumed, one with constant $\alpha_i^{(n)}$ and another with $\alpha_i^{(n)}$ linearly increasing with frequency (resulting with a constant damping ratio ζ). For each dataset, a number of two-phase numerical models of the analysed structure are created. In each model, an actuator position is assumed, at which the wave is excited and n sensors are established, at which the numerical wave signals $s_{i,j}^{(n)}$, $j = 1,2,\ldots,n$ are received. The specificity of numerical simulation of wave propagation is later described in detail in Section 3.3. For each signal, a cumulative energy functions $E_{i,j}^{(n)}$ are numerically computed using formula (6). Then, a set of b cumulative energy functions $E_{i,k}^{(s)}$, $k = 1,2,\ldots,b$ are calculated using formula (8) with different values of α_k and f_i. For each numerical energy function $E_{i,j}^{(n)}$ a synthetic energy function $E_{i,k}^{(s)}$ is fitted, allowing to determine the optimal mass proportionality coefficients $\alpha_{i,j}^{(n)}$. The fitting algorithm is based on the minimization of residual sum of squares (RSS [29]) between the functions, individually for each signal energy $E_{i,j}^{(n)}$.

The fitting procedure is as follows. First the signal energy function is normalised and the time limits for optimisation are established (Fig. 2a). Since the signal energy function is disturbed by the influence of the direct impact of the excitation, the initial part of the function must be truncated. Moreover, the final part of the signal, which is almost constant also must be eliminated to avoid false fitting of incorrect mass proportionality coefficients (this part does not differentiate significantly synthetic energy functions for different α coefficients). For this reason, two characteristic points in the signal energy are determined for the following energy levels: $E_0 = 0.01$ and $E_2 = 0.99$. The corresponding time instants are denoted as t_0 and t_2. Then, the midpoint t_1 between t_0 and t_2 is calculated. The reason for determining t_1 this way was the observation that the first half of the energy function include significant disturbances while the following part is smoother, allowing for more reliable fitting (as in example in Fig. 2a). The signal is cut between t_1 and t_2 establishing the time window Δt for optimisation. Independently, the set of synthetic energy functions for a specific range of mass proportionality coefficients are calculated and normalised (Fig. 2b). Since the synthetic signal energy function (8) is based on an exponential function, it is characterised by self-similarity, i.e., if cut for any time range (with constant time window) and normalised from 0 to 1, it will be the same, thus no additional editions are required for this functions. Then, the cut signal energy is translated through time axis on each synthetic energy curve and the RSS is calculated for each position of cut signal energy, using formula ([29]):

$$RSS_{i,j,k} = \sum \left(E_{i,j}^{(n)} - E_{i,k}^{(s)}\right)^2 \tag{9}$$

From all the RSS values, a minimum is selected, indicating the best fitted synthetic energy at a specific translation. As a result, $\alpha_{i,j}^{(n)}$ values are obtained. Since the distance between the sensor and actuator influences the amplitude of a direct wave, it is important to note, that sensors located closer to the actuator are characterised by higher damping. Thus, the values calculated for different sensors are not equal and require an averaging algorithm to obtain a single value of α that characterises the whole model. It was observed that α decreases exponentially with the distance from the sensor, thus it was assumed that the weighting algorithm should include the exponent of the distance x_j between sensor and actuator. Thus, the mean mass proportionality coefficient $\alpha_{a,i}^{(n)}$ for each dataset is expressed as:

$$\alpha_{a,i}^{(n)} = \frac{\sum_{j=1}^{n} e^{x_j} \alpha_{i,j}^{(n)}}{\sum_{j=1}^{n} e^{x_j}} \tag{10}$$

It is important to note that the obtained values of $\alpha_{a,i}^{(n)}$ significantly differs from the initial values assumed for the training datasets $\alpha_i^{(n)}$ (see Fig. 5 in later section 4.1.1). This is due to the fact that the wave signals are affected by the multiple reflection and diffraction of the wave at aggregates synthetically reducing the attenuation. What is more, this influence is different for different excitation frequencies f_i. For this reason, a correction algorithm is required. It was assumed that the corrected value of α can be calculated with respect to the formula:

$$\alpha_{c,i}^{(n)}(p,q,r) = r(f_i)^p \left(\alpha_i^{(n)}\right)^q \alpha_{a,i}^{(n)} \tag{11}$$

In the formula, r is a constant reduction coefficient, and p and q are constant exponents of frequency f_i (in kHz) and α_i (in rad/s), respectively. Ranges of p, q, and r coefficients are assumed and a corrected $\alpha_{c,i}^{(n)}$ is calculated for these ranges. Then, an absolute relative error $\delta\alpha$ between corrected and initial values is calculated for each estimated value of α:

$$\delta\alpha(p,q,r) = \left| \frac{\alpha_{c,i}^{(n)}(p,q,r) - \alpha_i^{(n)}}{\alpha_i^{(n)}} \right| \tag{12}$$

Next, a mean error is calculated including values from all analysed training datasets. The minimum error is searched to determine the

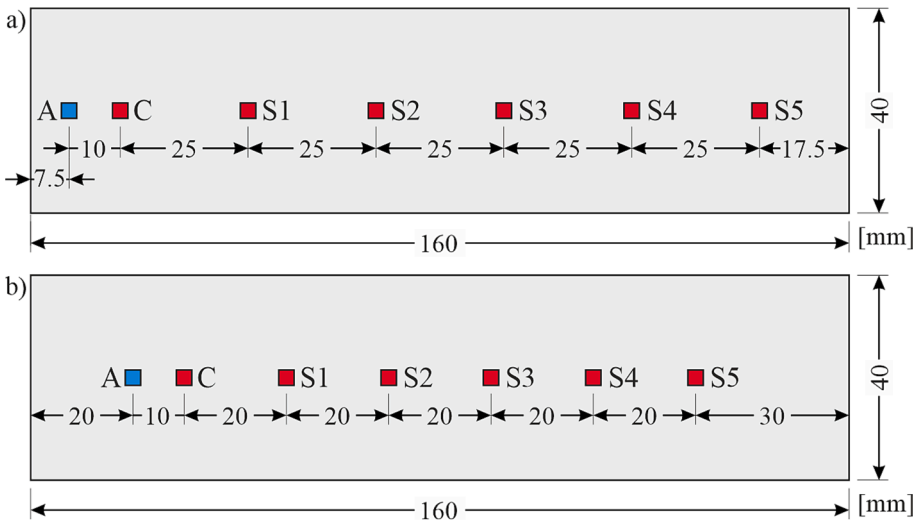

Fig. 3. Configuration of sensors: a) for sample #A; b) for samples #B1-4.

optimal values of p, q, and r. The above-described steps lead to the formula for estimation of α for the specific geometry of sample, material parameters and sensor locations.

The second stage (II) is the experimental investigation. The set of wave propagation measurements are conducted for the physical model of the sample that was reflected in the numerical simulation, for the same excitation frequencies f_i. It is important to note that the experimental $\alpha_i^{(e)}$ values are unknown. As a result, a set of experimental wave signals $s_{i,j}^{(e)}$, $j = 1,2,\ldots,n$ is obtained, for which cumulative energy functions $E_{i,j}^{(e)}$ are calculated using formula (6). Further steps are analogous to numerical calculations. The set of $\alpha_{i,j}^{(e)}$ values are calculated based on the comparison with synthetic energy functions, using formula (9). Then, the averaged value $\alpha_{a,i}^{(e)}$ is obtained using formula (10). Since the initial values of α remain unknown, the correction formula obtained from the numerical calculations is used with the assumption that the corrected value $\alpha_{c,i}^{(e)}$ is equal to the unknown value $\alpha_i^{(e)}$. Thus, formula (11) changes form to:

$$\alpha_{c,i}^{(e)} = \left(r(f_i)^p \alpha_{a,i}^{(e)}\right)^{\frac{1}{1-q}} \tag{13}$$

The obtained values of $\alpha_{c,i}^{(e)}$ are then used as a testing dataset for the stage III.

The testing dataset consisting of m values of f_i and $\alpha_i^{(ne)} = \alpha_{c,i}^{(e)}$ is used to verify the proposed algorithm in stage III. Numerical simulations in the same two-phase numerical models as in stage I are performed for each pair of values. The number of n signals $s_{i,j}^{(ne)}$ is collected and their cumulative energy functions $E_{i,j}^{(ne)}$ are numerically computed using formula (6). The RSS-based optimisation algorithm used previously (formula (9)) is introduced to determine a set of $\alpha_{i,j}^{(ne)}$ values. The values are averaged using formula (10), allowing to obtain $\alpha_{a,i}^{(ne)}$ values. The same correction formula (11) as in the numerical stage is used to determine the corrected $\alpha_{c,i}^{(ne)}$ values. These values can be verified by calculating the error with respect to the initial values $\alpha_i^{(ne)}$. If the verification is successful, i.e., the error is sufficiently low, the corrected values treated as testing dataset are final values that can be used for further modelling $\alpha_{f,i} = \alpha_i^{(ne)} = \alpha_{c,i}^{(e)}$. In the case of a different object of study (e.g., different material, sample geometry or sensor configuration), the algorithm can be repeated to obtain specific correction functions.

4. Materials and methods

4.1. Object of research

The research was conducted on concrete beams with a length of 160 mm and a square cross section with dimensions of 40 × 40 mm^2. The samples were cut from a concrete prism with the dimensions of 100 × 100 × 500 mm^3 to avoid the effect of separation of ingredients that could occur in a small mould. The concrete mix was prepared from: cement type CEM I 42.5R (330 kg/m^3), water (165 kg/m^3), aggregate 0–2 mm (710 kg/m^3), aggregate 2–8 mm (664 kg/m^3), aggregate 8–16 mm (500 kg/m^3), and super-plasticizer (0.7 % of the cement content). Five samples were prepared for different purposes. First (#A) was used to identify the attenuation characteristics in undamaged state, and another four denoted as #B1-#B4 were used to observe the changes in attenuation during the bending test.

4.2. Experimental investigations

The samples were tested using guided wave propagation method under different conditions. Sample #A was tested without external load, situated freely on the laboratory table. Independently, samples of type #B were subjected to three-point bending test using universal testing machine Zwick/Roell Z10. The distance between the supports was 120 mm. Each specimen #B1-4 was tested with the same testing parameters. Initially, the preload of 50 N was applied and the bending process was conducted with a constant displacement rate of 0.05 mm/min until reaching the limit displacement of 0.5 mm, resulting with a total test time of 600 s. The input ultrasonic signals were generated using an arbitrary waveform generator and amplified by a high voltage amplifier. The excitation was a wave packet modulated from a 5-cycle sinusoidal function using the Hann window. Seven multilayer piezoelectric transducers NAC2024 manufactured by Noliac were used to excite and collect propagating elastic waves. One of the transducers acted as an actuator (A), another one (C) was a control sensor used to trigger measurements and the remaining ones operated as main sensors (S1-S5) for the actual signal collection (number of sensors $n = 5$). The configuration of sensors for both sample types is presented in Fig. 3. The sensors were placed on the surface of the sample with even spacing to record wave signals at different locations. The aim was to collect as much information as possible about propagating waves and characterize the wave attenuation at various distances from the actuator (a single signal at a specific point would not adequately represent the behaviour of waves). Ultrasonic wave signals of 5 ms length were recorded using a digital

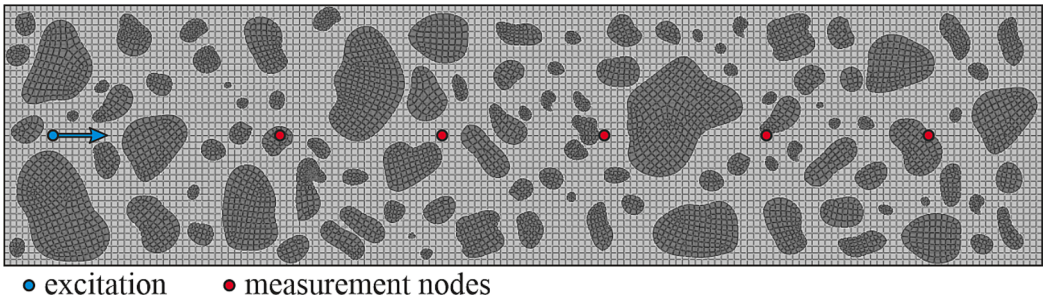

Fig. 4. Numerical model of analysed concrete beam with sensor configuration of sample #A.

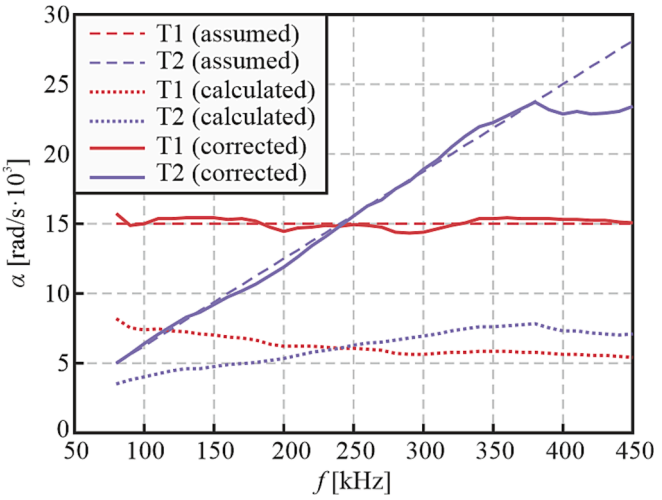

Fig. 5. Mass proportionality coefficients in relation to frequency from training datasets (assumed $\alpha_i^{(n)}$, calculated $\alpha_{a,i}^{(n)}$ and corrected $\alpha_{c,i}^{(n)}$ values) – simulations with sensor configuration for sample #A.

oscilloscope with a sampling frequency of 8 MHz.

In the case of sample #A (Fig. 3a), several measurements were consecutively conducted with different wave frequencies in a range of 80–450 kHz with a step of 10 kHz, resulting in 38 independent measurements. The samples #B1-4 investigated during three-point bending were tested with different sensor configuration (Fig. 3b) to verify the ability of the developed algorithm to test under various conditions. The sensors were located with smaller spacing than in sample #A to better characterize progressing crack that was expected to arise in the central part of the sample. Automatic signal excitation and acquisition was assumed with a constant time step of 1 s. It is important to note that the excitation frequency alternated between two values (100 kHz and 300 kHz for samples #B1-2 and 200 kHz and 400 kHz for samples #B3-4). This operation resulted with almost simultaneous (shifted in time by 1 s) measurement of wave propagation with two different frequencies in the same sample. As a result, two sets of 300 signals with time step of 2 s were obtained for each sample of type #B.

4.3. Numerical modelling

A number of numerical models were prepared to simulate the wave propagation in samples #A and #B. The analysed beam was modelled in plane stress using Abaqus/Explicit software. A simplified two-phase heterogeneous model (Fig. 4) was prepared using the geometry of a slice of the analysed beam with real aggregate arrangement. The homogeneous isotropic material model was adopted for each phase (mortar and aggregates). The mechanical parameters of each phase are presented in Table 1. All elements were discretised with element type CPS4R, i.e., a 4-node bilinear plane stress quadrilateral finite element

Table 1
Mechanical parameters of phases in numerical model of analysed beam.

Phase	Density ρ [kg/m^3]	Young's Modulus E [GPa]	Poisson's ratio ν [–]
mortar	2000	40	0.2
aggregate	2600	70	0.3

with reduced integration and hourglass control. The global size of the finite element mesh was assumed to be 1 mm for both phases with local refinement in the area of aggregate irregularities. The mesh size was chosen based on the requirement of sufficient representation of wave behaviour, i.e., at least 10 nodes for the shortest wave of interest (after [30]). The calculations of wave propagation were conducted using explicit algorithm of the central difference method with a fixed time step of 10^{-7} s, so that the cycle of the highest frequency wave was covered by at least 20 integration points (according to [31]). The excitation signal had a form of a horizontal concentrated force with varying amplitude, compatible with the wave packet signal used in experimental investigations. The horizontal acceleration signals were collected in a number of nodes located in positions reflecting the configuration of PZT sensors in experiments (independently in simulations of sample #A and samples of type #B).

The Rayleigh proportional damping model with a non-zero mass proportionality coefficient α was assumed to obtain attenuation of the wave signals (stiffness proportionality coefficient β equal to 0). An equal $\alpha_i^{(n)}$ was assumed for both concrete phases (mortar and aggregates) to simplify the modelling. Initially, training models were prepared in a frequency range f_i between 80 kHz and 450 kHz with a step of 10 kHz (covering the same frequency range as in experimental investigations of sample #A). Two datasets were used: the first (T1) with constant $\alpha_i^{(n)} =$ 15 000 rad/s for each frequency and the second (T2) with constant damping ratio $\zeta = 0.49736$ %, resulting in linearly distributed $\alpha_i^{(n)}$ in the range between 5000 rad/s for 80 kHz and 28125 rad/s for 450 kHz. These training datasets were used for numerical simulations of both types of samples (#A and #B), independently. Numerical calculations were also performed on test datasets obtained from the experimental measurements.

5. Results and discussion

5.1. Determination of mass proportionality coefficients in sample #A

5.1.1. Training datasets in numerical model

As a first step of the analysis, $m = 38$ simulations were performed with each training dataset T1 and T2 (each simulation with different frequency f_i from range between 80 kHz and 450 kHz). The numerical signals obtained from the simulations were processed using the described algorithm (Fig. 1) in stage I. For each signal, a cumulative energy function $E_{i,j}^{(n)}$ was determined and the $\alpha_{i,j}^{(n)}$ coefficient was calculated. The range of possible α_k values was assumed to be between 1000

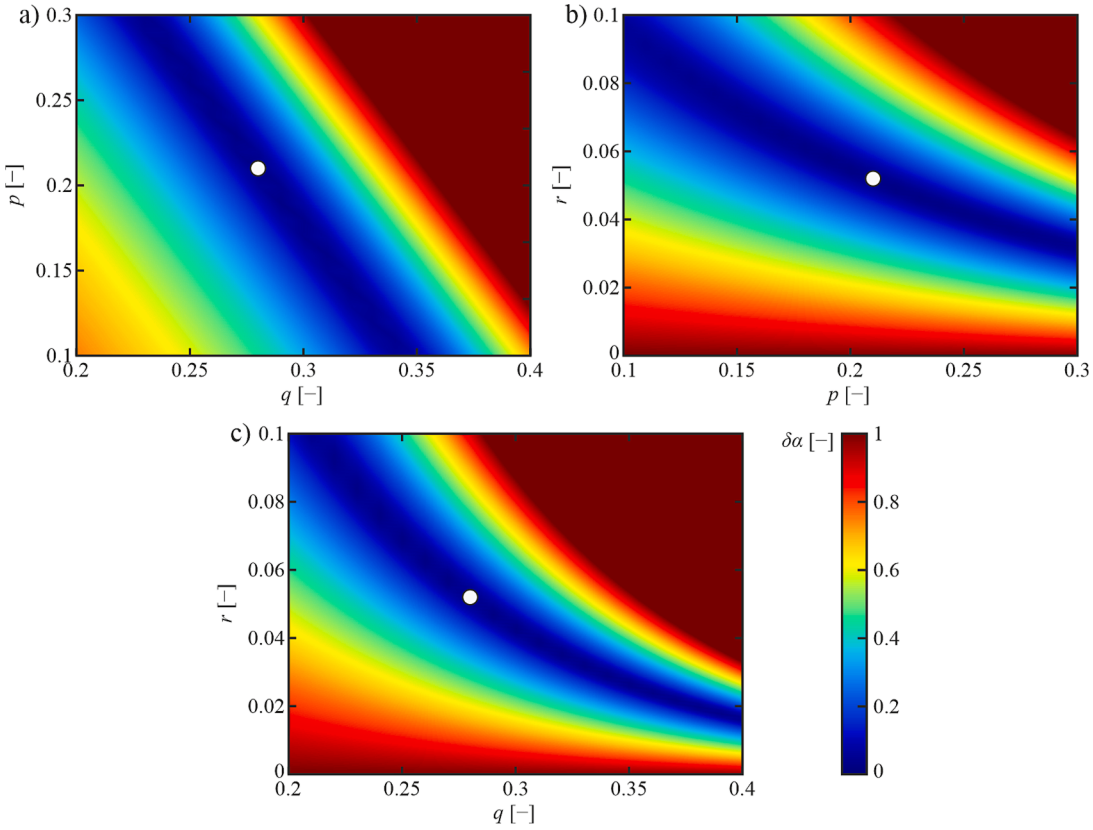

Fig. 6. Sections of minimised error function $\delta\alpha$ (sample #A): a) $\delta\alpha$ vs. p and q for $r = 0.052$; b) $\delta\alpha$ vs. p and r for $q = 0.28$; c) $\delta\alpha$ vs. q and r for $p = 0.21$.

rad/s and 60 000 rad/s with the step of 100 rad/s, whereas the possible shift of the energy function was between 0 and 1 ms with the step of 0.0025 ms. The calculations were performed individually for each sensor and the $\alpha_{i,j}^{(n)}$ values were finally averaged using formula (10) obtaining $\alpha_{a,i}^{(n)}$. The results of the calculations are presented in Fig. 5. It can be seen that the calculated $\alpha_{a,i}^{(n)}$ values (dotted lines) differ significantly from those assumed for the numerical simulations $\alpha_i^{(n)}$ (dashed lines) for both training datasets T1 and T2. These discrepancies are due to the heterogeneous structure of the sample which leads to multiple reflections and interferences of the waves, apparently reducing the attenuation. In the case of dataset T1 (with constant $\alpha_i^{(n)}$) it can be seen that the error increases with frequency. Furthermore, the error also increases with $\alpha_i^{(n)}$, as can be seen from the results from dataset T2. Thus, both frequency and α have an influence on the error of calculation. For this reason, to eliminate the error, the model calibration was performed with a correction function, according to formula (11).

The optimisation procedure was performed in the range between 0 and 2 for all coefficients p, q, and r with the step of 0.01 for p and q and the step of 0.001 for r (to obtain the same accuracy, because the obtained r values were one order lower). All the coefficients had positive values, because the error between assumed $\alpha_i^{(n)}$ and calculated $\alpha_{a,i}^{(n)}$ values increased with both frequency and α. The error function $\delta\alpha$ was calculated for all values of the coefficients p, q, r, and the global minimum was found for $p = 0.21$, $q = 0.28$ and $r = 0.052$ (including the mean error for both training datasets T1 and T2). As the minimised $\delta\alpha$ function is a function of three variables it is not possible to show it in a single figure in its 4D representation. Thus, three different sections have been prepared as coloured maps (Fig. 6). The range of the coefficients p, q, r was reduced to better show the localisation of the minimum. The minimum error was equal to 2.93 %, which is an acceptable value. After determining the optimal coefficients, additional calculations of α were performed to verify the efficiency of the correction formula for both training datasets. The corrected values $\alpha_{c,i}^{(n)}$ are presented in Fig. 5 (solid lines). As expected, the value of α increases with frequency. It can be clearly seen that the corrected values $\alpha_{c,i}^{(n)}$ are similar to the assumed ones $\alpha_i^{(n)}$. The mean error for dataset T1 is 2.05 %, whereas for T2 it is 3.80 %. The error in the second dataset is higher due to the significant difference in the higher frequency range, which will be discussed further in detail.

5.1.2. *Experimental results*

The signals obtained from the experimental measurements performed on sample #A were processed as described in stage II of the algorithm. The cumulative energy functions $E_{i,j}^{(e)}$ were fitted to synthetic energy functions $E_{i,k}^{(s)}$ and $\alpha_{i,j}^{(e)}$ values were calculated. The examples of fitting for signals from all sensors S1-S5 at representative frequencies (150 kHz and 400 kHz) are presented in Fig. 7.

In the optimisation range (marked by the shaded area) the experimental cumulative energy functions are smooth and clearly correlate with synthetic ones. However, the disturbed character of the experimental functions is clearly visible at the initial part, suggesting that optimisation in a limited time domain was justified. It is particularly visible at the lower frequency (150 kHz) for sensors located near the actuator, because the influence of the direct wave is much more pronounced. The synthetic $E_{i,k}^{(s)}$ and experimental $E_{i,j}^{(e)}$ energy functions differ significantly at the initial part. This effect is less visible for the 400 kHz frequency because higher frequency waves have shorter wavelengths and can interact with structural discontinuities of smaller size, making the energy functions smoother. As a result, the correlation between the experimental and synthetic functions is higher in the whole time range. What is more, higher frequencies are characterised by higher attenuation, thus time range is shorter for 400 kHz than for 150 kHz.

The mass proportionality coefficients obtained from the optimisation

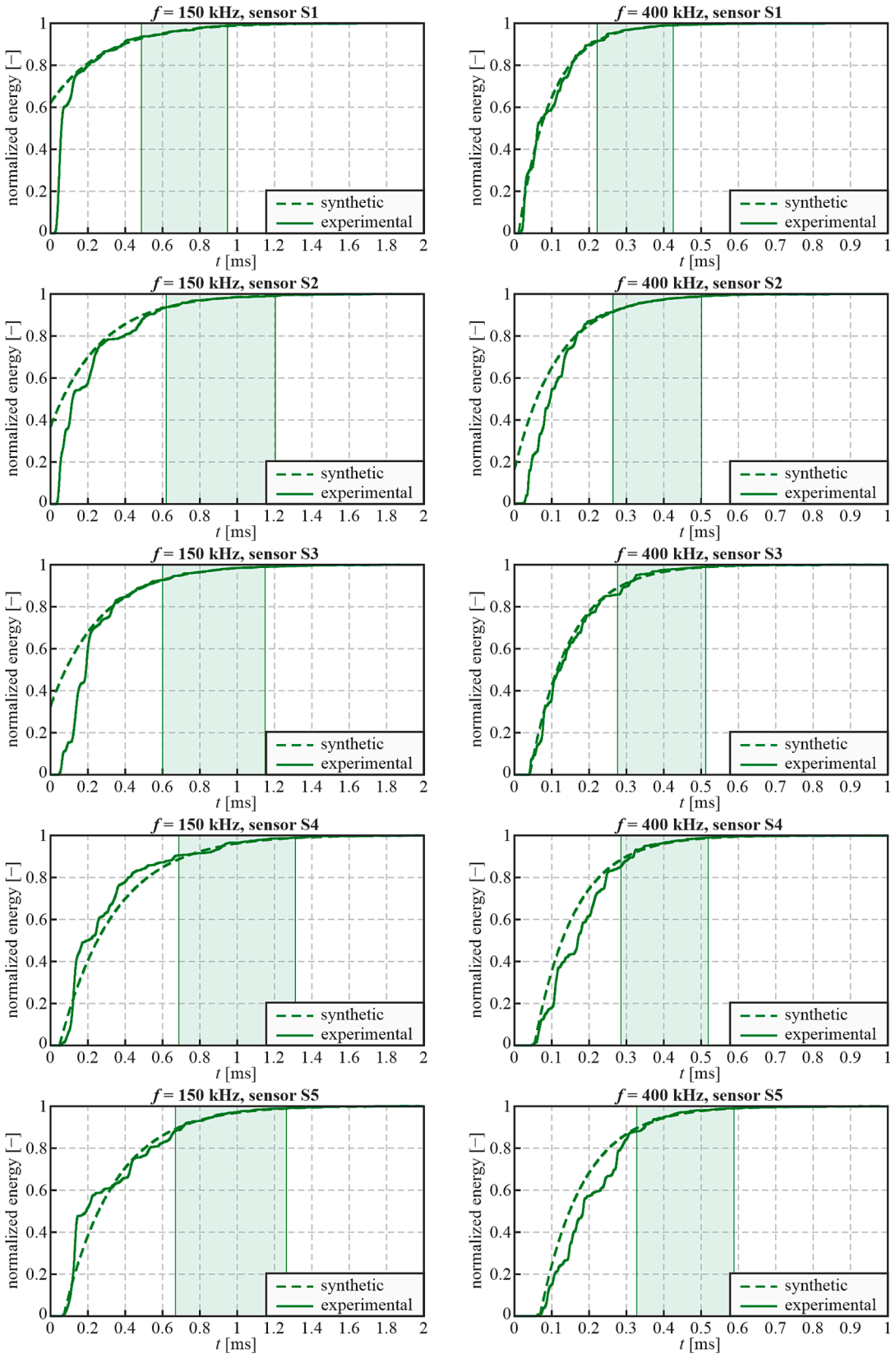

Fig. 7. Cumulative energy functions from experiment performed on sample #A based on ultrasonic signals from sensors S1-S5 and fitted synthetic energy for 150 kHz and 400 kHz.

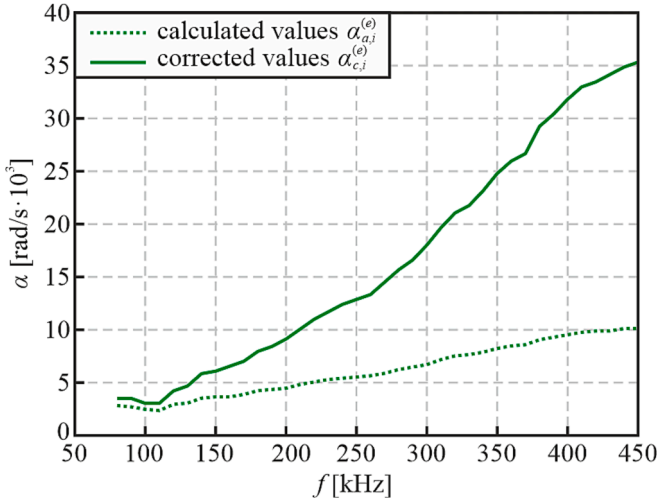

Fig. 8. Mass proportionality coefficients in relation to frequency from experimental measurements – comparison of values without $\alpha_{a,i}^{(e)}$ and with correction ($\alpha_{c,i}^{(e)}$).

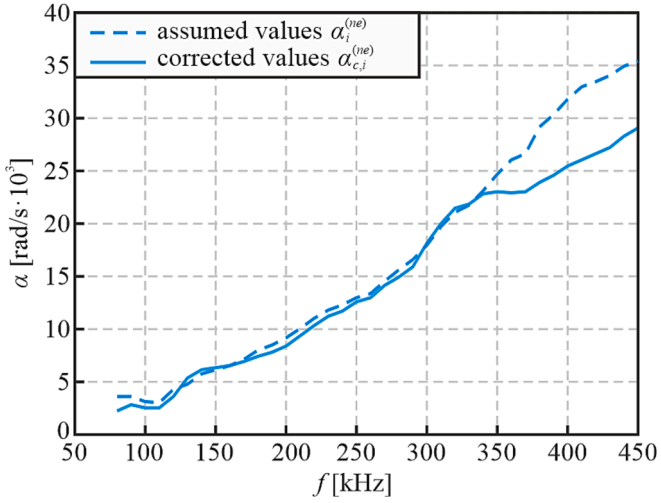

Fig. 9. Mass proportionality coefficients in relation to frequency in testing dataset obtained for sample #A – comparison of assumed values $\alpha_i^{(ne)} = \alpha_{c,i}^{(e)}$ (from experiments) and calculated using correction algorithm $\alpha_{c,i}^{(ne)}$.

must be further corrected. Since the $\alpha_i^{(e)}$ coefficients of the tested material are unknown, the correction function determined in the previous section was used. The comparison of calculated $\alpha_{a,i}^{(e)}$ and corrected $\alpha_{c,i}^{(e)}$ values is shown in Fig. 8. As in the previous results, it is evident that the difference between calculated and corrected values is significant and increases with frequency and mass proportionality coefficient. The variation of α in relation to frequency is close to linear, which makes the choice of the training dataset T2 with linearly increasing α reasonable. Some deviation from a general trend can be seen in the lower frequency range (80–120 kHz), where α slightly decreases, and in the high-frequency range (400–450 kHz), where the increase of α is less pronounced. It should be noted that the obtained values of $\alpha_{c,i}^{(e)}$ differs from the ones used in training datasets, so it is important to check whether the correction algorithm is suitable for calculating these values.

5.1.3. *Verification of calculations with testing dataset*

The determined corrected values of the mass proportionality coefficient $\alpha_{c,i}^{(e)}$ were used as a testing dataset $\alpha_i^{(ne)}$ for numerical simulations. The signals obtained from all 38 numerical models were processed to obtain $\alpha_{i,j}^{(ne)}$ coefficients which were then averaged and corrected using the same correction function as in the previous steps. The comparison of assumed values $\alpha_i^{(ne)}$ (testing dataset, dashed line) and those calculated with correction $\alpha_{c,i}^{(ne)}$ (solid line) is presented in Fig. 9. The mean absolute error equals 10.3 % in the whole range. However, it is important to note that the differences are significant at higher frequencies (above 350 kHz), where the general linear trend is much more disturbed than in the experimental results discussed in the previous section. In the frequency range between 100 kHz and 350 kHz, the error equals 4.87 %, which is a satisfactory value, so the results are reliable in this range, thus experimental values can be considered final result of the calculations: $\alpha_{f,i} = \alpha_i^{(ne)} = \alpha_{c,i}^{(e)}$.

The results for higher frequencies are not efficient because of the wave interaction with individual aggregates. In the case of highly heterogeneous materials, it is important to consider the internal structure of tested sample. For lower frequencies, the location of aggregates does not affect the wave propagation signals as long as the aggregates are evenly distributed and their content in the mortar does not change. The waves can propagate through the sample as a whole medium without significant interaction with particular aggregates, which is possible if the wave is long enough. As the frequency increases, the wavelength decreases, thus the waves can be diffracted by particular aggregates, significantly affecting the wave signals. In order to better analyse this effect, the lengths of the waves considered in the current study were calculated. The time of flight (TOF) of the wave was determined as the difference between the time zero of the signals from sensors C and S5 measured on sample #A. Knowing the distance between the two sensors (L = 125 mm), the wave velocity c was calculated by dividing L by TOF. The wave velocity for each considered frequency is presented in Fig. 10a. Knowing the velocity c and frequency of the wave f, the wavelength λ was calculated by dividing the velocity by the frequency. The relationship between wavelength and frequency is shown in Fig. 10b. The length of the wave with 350 kHz frequency equals 13.7 mm. Considering the fact that the largest aggregate size is 16 mm and the distance between particular aggregates can be smaller, the wave with frequency higher than 350 kHz can diffract at the aggregates affecting the wave signals.

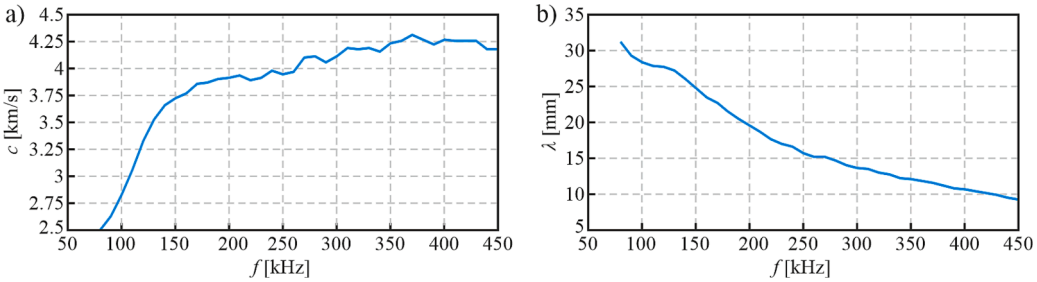

Fig. 10. Characteristics of wave propagating in analysed concrete sample #A: a) group velocity vs. frequency; b) wavelength vs. frequency.

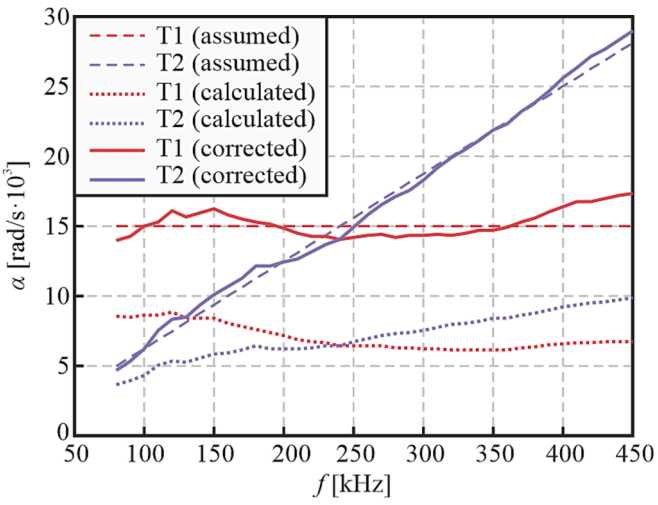

Fig. 11. Mass proportionality coefficients in relation to frequency from training datasets (assumed $\alpha_i^{(n)}$, calculated $\alpha_{a,i}^{(n)}$ and corrected $\alpha_{c,i}^{(n)}$ values) – simulations with sensor configuration for sample #B.

These diffractions are reflected in wave signals as additional wave packets, increasing the amplitude and artificially reducing the signal attenuation. In this case, the material can no longer be considered as homogenized and its macrostructure needs to be adequately represented in numerical simulations. This allows stating that the developed algorithm can only be efficient in the specific frequency range. For any particular case of different material, the above-described analysis of the interaction of the wave with the internal structure of the sample (comparison between the shortest wavelength of interest and the aggregate size) must be performed to ensure the reliability of the proposed procedure.

5.2. Determination of mass proportionality coefficients in samples of type #B

5.2.1. Training datasets in numerical model

Similarly to the analysis of sample #A, the training datasets T1 and T2 were used to determine the correction algorithm for samples of type #B, based on numerical simulations in models with the sensor configuration reflecting scheme presented in Fig. 3b. The results of the calculations are shown in Fig. 11. Similarly to the outcome for sample #A, the calculated values $\alpha_{a,i}^{(n)}$ (without correction, dotted lines) are significantly lower than the assumed ones $\alpha_i^{(n)}$ (dashed lines), thus correction was required.

The calculation of the correction coefficients p, q, r was performed for the same range as for sample #A, i.e., between 0 and 2. The global minimum of $\delta\alpha$ function was found for $p = 0.26$, $q = 0.22$, and $r = 0.063$. The sections of the minimised $\delta\alpha$ function are presented in Fig. 12. The minimum error was 4.46 %, which is acceptable. Using the determined correction coefficients, corrected values of the mass proportionality coefficient $\alpha_{c,i}^{(n)}$ were calculated for both training datasets. The results are presented in Fig. 11 (solid lines). The mean error for training dataset T1 was 5.37 %, whereas for dataset T2 it was 3.56 %. The largest errors are present for higher frequencies, as was the case for sample #A, however,

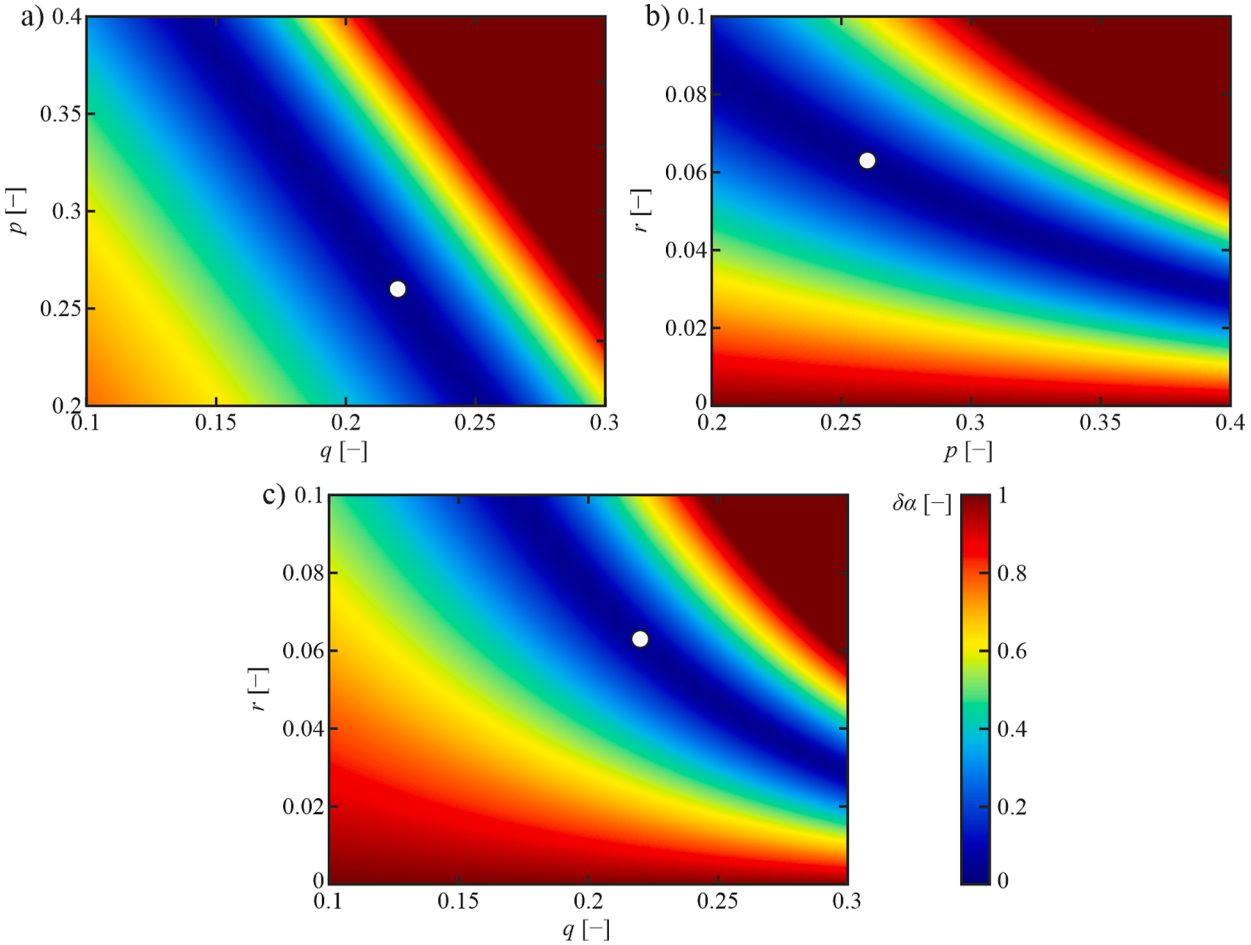

Fig. 12. Sections of minimized error function $\delta\alpha$ (sample #B): a) $\delta\alpha$ vs. p and q for $r = 0.063$; b) $\delta\alpha$ vs. p and r for $q = 0.22$; c) $\delta\alpha$ vs. q and r for $p = 0.26$.

Table 2
Mass proportionality coefficients from experimental measurements of samples #B1-4 – comparison of averaged values without correction $\alpha_{a,i}^{(e)}$, values with correction, used then as a testing dataset $\alpha_{c,i}^{(e)} = \alpha_i^{(ne)}$, and verified by numerical simulations $\alpha_{c,i}^{(ne)}$ (all values in rad/s).

f [kHz]		#B1	#B2	#B3	#B4
100	$\alpha_{a,i}^{(e)}$ – averaged (without correction)	2774	2663	–	–
	$\alpha_{c,i}^{(e)}=\alpha_i^{(ne)}$ – averaged and corrected	3479	3303	–	–
	$\alpha_{c,i}^{(ne)}$ – verified by simulations	2848	2624	–	–
200	$\alpha_{a,i}^{(e)}$ – averaged (without correction)	–	–	5407	4862
	$\alpha_{c,i}^{(e)}=\alpha_i^{(ne)}$ – averaged and corrected	–	–	10,316	9004
	$\alpha_{c,i}^{(ne)}$ – verified by simulations	–	–	10,399	9031
300	$\alpha_{a,i}^{(e)}$ – averaged (without correction)	7727	7416	–	–
	$\alpha_{c,i}^{(e)}=\alpha_i^{(ne)}$ – averaged and corrected	18,667	17,708	–	–
	$\alpha_{c,i}^{(ne)}$ – verified by simulations	18,210	17,106	–	–
400	$\alpha_{a,i}^{(e)}$ – averaged (without correction)	–	–	12,207	11,629
	$\alpha_{c,i}^{(e)}=\alpha_i^{(ne)}$ – averaged and corrected	–	–	36,921	34,695
	$\alpha_{c,i}^{(ne)}$ – verified by simulations	–	–	34,407	33,711

this time the differences are more pronounced for dataset T1.

5.2.2. Experimental results

The experimental signals measured on samples #B were processed as presented in stage II of the algorithm. To enable comparison with the results of sample #A, only the first signals in each dataset (without an insignificant value of external load) were analysed at this step. Cumulative energy functions $E_{i,j}^{(e)}$ were calculated and fitted to synthetic functions $E_{i,k}^{(s)}$ to determine mass proportionality coefficients $\alpha_{i,j}^{(e)}$. The obtained values were averaged and corrected using correction function determined in the previous section. The comparison of the calculated $\alpha_{a,i}^{(e)}$ and corrected $\alpha_{c,i}^{(e)}$ values is presented in Table 2. It can be clearly seen that the values obtained are similar between samples tested with the same frequency. To verify the performed calculations, the obtained corrected values were assumed as a testing dataset for numerical simulations.

5.2.3. Verification of calculations with testing dataset

The determined corrected values $\alpha_{c,i}^{(e)}$ were used for numerical calculations as testing dataset $\alpha_i^{(ne)}$. The numerical wave signals were processed to determine the corrected values $\alpha_{c,i}^{(ne)}$ with the established correction function. The results of the calculations are presented in Table 2. The mean absolute error between the values assumed for the simulations and the corrected ones is equal to 6.9 %, which can be considered sufficiently low. This means that the correction function did not significantly change these values, so the mass proportionality coefficients used for the testing dataset are the final result of the calculations, i.e., $\alpha_{f,i} = \alpha_i^{(ne)} = \alpha_{c,i}^{(e)}$.

5.3. Comparison of attenuation between samples #A and #B

The values of the mass proportionality coefficients $\alpha_{f,i}$ obtained for samples #B were compared with the ones calculated for sample #A. For each of four frequencies (100 kHz, 200 kHz, 300 kHz, and 400 kHz), the mean value of α was calculated. The comparison is presented graphically in Fig. 13, and the values are shown in Table 3. The mean error for all frequencies equals 6.7 %. The highest differences are observed for the highest frequency (400 kHz), however, as stated previously, the proposed algorithm can be inefficient for frequencies above 350 kHz. Excluding the highest frequency, the mean error reduced to 4.8 %. A good agreement between the mass proportionality coefficients obtained from samples with different sensor configurations proves the efficiency of the developed procedure.

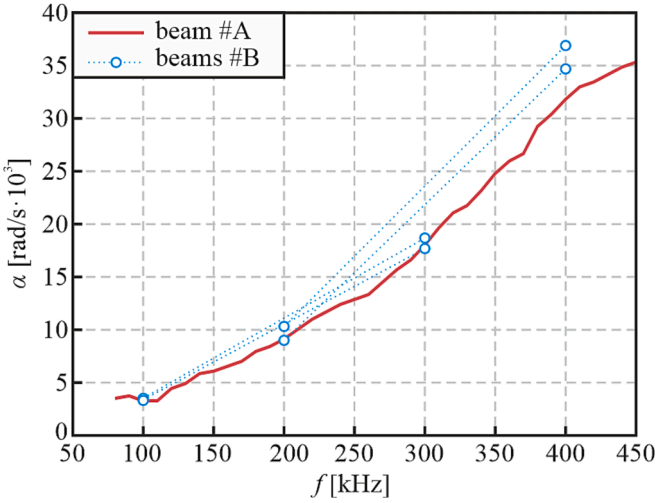

Fig. 13. Comparison between mass proportionality coefficients $\alpha_{f,i}$ calculated for beam #A and beams #B.

Table 3
Comparison of mass proportionality coefficients $\alpha_{f,i}$ from experiments performed on samples #A and #B (all values in rad/s).

f [kHz]	#A	Mean #B	Error of #B in relation to #A
100	3141	3391	8.0 %
200	9183	9660	5.2 %
300	17,987	18,188	1.1 %
400	31,793	35,808	12.6 %

5.4. Identification of attenuation changes during bending test

All experimental signals measured on samples #B (two sets for two different wave frequencies, each consisting of 300 signals) were processed to observe the mass proportionality coefficient changes during the three-point bending test. Cumulative energy functions were determined and fitted to synthetic functions to find optimal α coefficients. First, α was assumed to be between 1000 rad/s and 60 000 rad/s with the step of 100 rad/s. The possible time shifts were assumed to be in the range from 0 to 1 ms with a step of 0.0025 ms. However, to better show subtle changes of α during bending test, the calculations were repeated with the accuracy of α enhanced to 10 rad/s, but in the reduced range (α determined in first calculations ± 200 rad/s). The accuracy of the time shift was also improved (to 0.0005 ms). The finally obtained α values were averaged and corrected using the correction function determined in section 4.2.1.

The calculated mass proportionality coefficients for both frequencies and the force–time curve for all beams are presented in Fig. 14. It can be seen that most of the charts show only slight changes of α in the first part of the test, before reaching the peak load. The 100 kHz frequency in sample #B1 (Fig. 14a) shows a significant disturbance between 80 s and 170 s of the test. This could be the effect of local micro-cracking of concrete in this specimen. The 300 kHz frequency is almost constant before the peak with a slight increase near the peak. This increase may

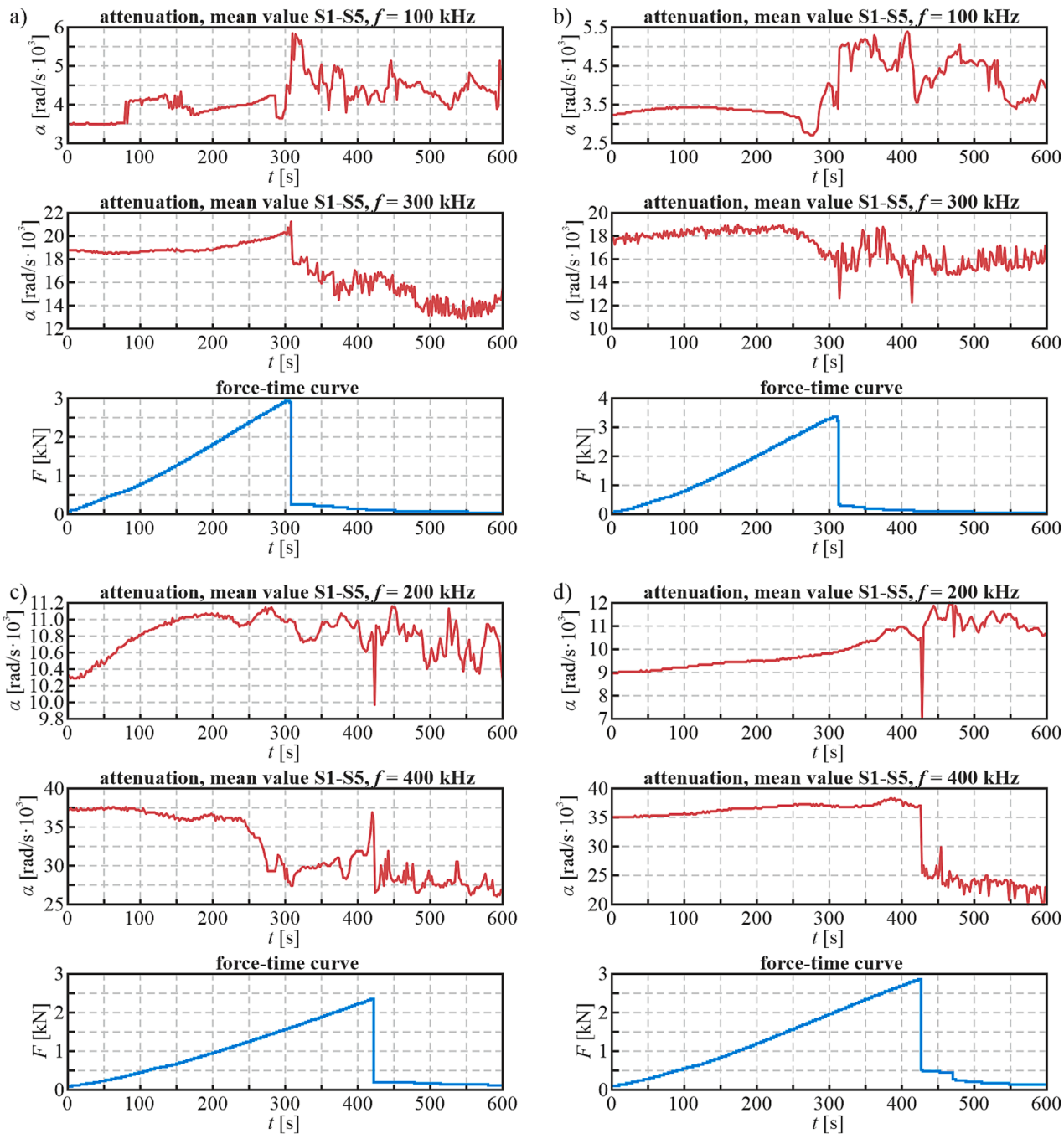

Fig. 14. Attenuation changes (mean values from all sensors) in beams of type #B during 3-point bending test and force–time curves: a) beam #B1, b) beam #B2, c) beam #B3, d) beam #B4.

be related to the change in stress in the material under bending. The evolution of α in beam #B2 (Fig. 14b) does not indicate any significant changes for either frequency. A slight increase is initially observed, but the α decreases near the peak. In the case of frequency 200 kHz for sample #B3 (Fig. 14c), a significant increase in α can be observed and then there are some increases and decreases, possibly due to the formation of local discontinuities in the internal structure of the beam. The 400 kHz frequency does not vary meaningfully in the initial part, however, some disturbances are visible in the same time instances as for the 200 kHz frequency. The sample #B4 (Fig. 14d) shows a smooth increase in α for both frequencies before the peak. The behaviour of all samples after reaching the peak load is unpredictable due to the formation and propagation of macro-cracks, indicating progressed mechanical degradation. The values of α vary significantly after peak load for all samples. This significant variation is related to the major changes in the internal structure of samples. Any changes in the α functions are not related to changes in the wave attenuation itself but results from the presence of defects that lead to multiple reflections of the wave, significantly altering the signals.

To better discuss the behaviour of the samples, the mass proportionality coefficient was calculated for the signals from all sensors and plotted separately in Fig. 15. It can be clearly seen that the individual sensors show different changes of α during the test. For example, the local disturbances observed for sample #B1 for frequency 100 kHz (Fig. 15a) are visible mainly in sensors S3 and S4 that are close to the centre of sample, where the crack occurred. Sensors S1, S2, and S5 do

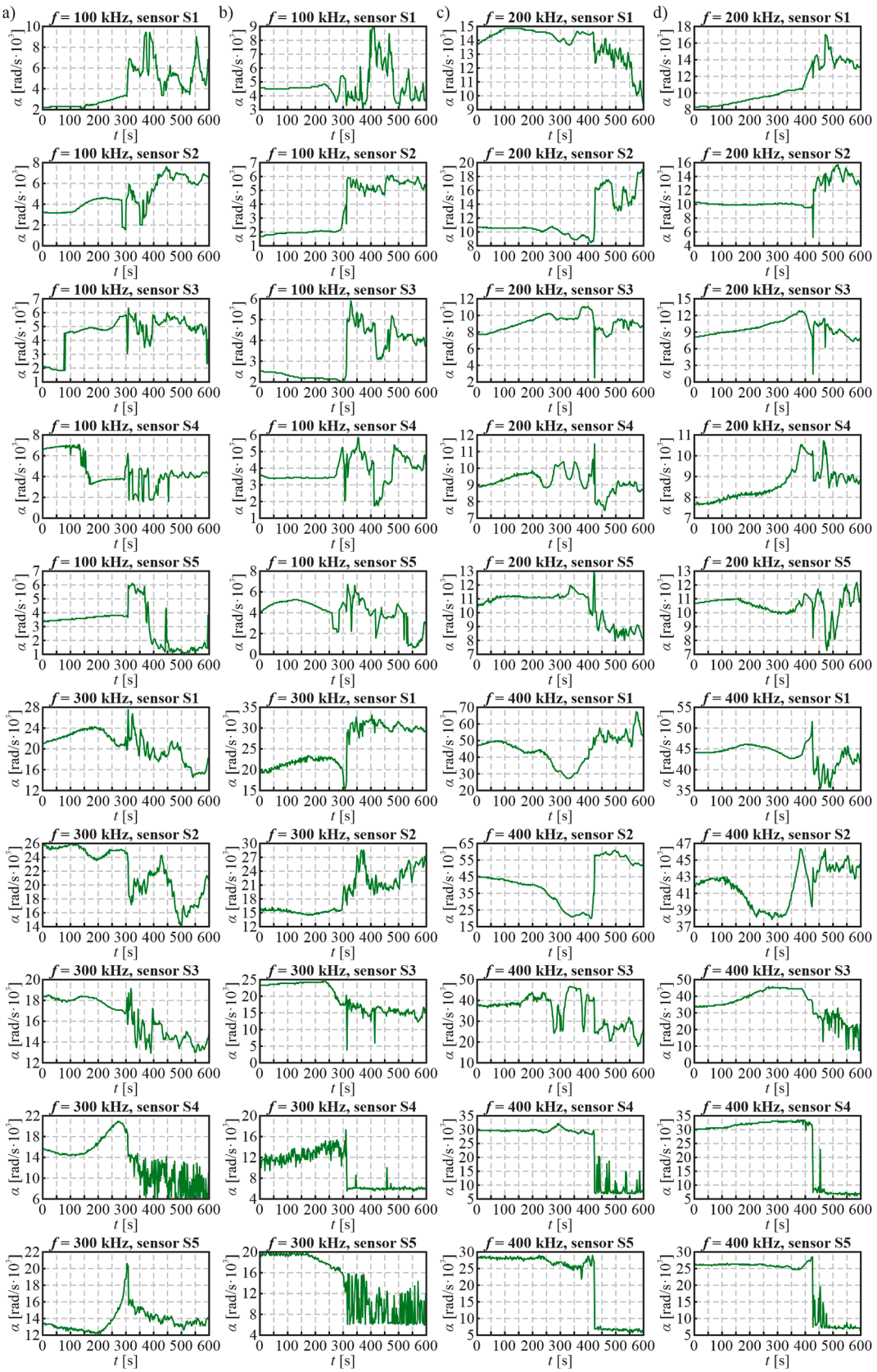

Fig. 15. Attenuation changes in sensors S1-S5 in beams of type #B during 3-point bending test: a) beam #B1, b) beam #B2, c) beam #B3, d) beam #B4.

not indicate any significant variation in α before peak. The sensors S1-5 for the 300 kHz frequency for the same sample show some growths and drops, however, mean value was almost constant (Fig. 14a). Similarly, particular sensors for both frequencies 100 kHz and 300 kHz for sample #B2 (Fig. 15b) shows different changes before peak load, but the mean values did not indicate any meaningful changes (Fig. 14b). Both frequencies in sample #B3 (Fig. 15c) show some local disturbances for all sensors, which were reflected in mean values (Fig. 14c). Similarly to the 300 kHz frequency for sample #B1, some sensors for both frequencies in sample #B4 (Fig. 15d) indicate increase in α, while the others show decrease, however, the mean values are only slightly increasing (Fig. 14d). This proves that the attenuation behaviour of material varies differently in particular locations due to the non-uniform distribution of cracks throughout the sample, but the global response does not change significantly. This observation proves that characterisation of attenuation in heterogeneous materials by a single signal is not sufficient and that a series of measurements performed at different locations is required. However, the wave attenuation is affected by changes in the internal structure of tested medium, so it can be stated that attenuation can be a promising factor in identifying the progression of damage in concrete elements. It should also be noted that the mass proportionality coefficient was determined using the correction function obtained from the numerical simulations on the intact sample (without structural damage). Thus, the results need to be treated qualitatively, because in the case of progressive damage, the correction function may change due to the presence of cracks that behave as additional wave scatterers influencing the ultrasonic wave signals. To adequately determine the mass proportionality coefficient at different levels of mechanical degradation, accurate models reflecting crack propagation should be developed, e.g., based on digital image correlation measurements during the bending test. The aim of the current work, however, was to prove the sensitivity of attenuation to the presence of structural damage, which was achieved. Further works dedicated to quantitative analysis of changes of Rayleigh coefficients are planned.

6. Conclusions

The paper presented the newly developed procedure for the identification of attenuation in heterogeneous material based on ultrasonic wave propagation measurements. The main objective was to determine the mass proportionality coefficient for further modelling of wave attenuation using Rayleigh proportional damping. The main findings are presented below.

The proposed algorithm allowed automated calculation of the mass proportionality coefficient of concrete based on changes of cumulative signal energy. Thanks to the normalization of the cumulative signal energy, the developed method did not require analysis of differences between amplitudes of signals collected by individual sensors what eliminated the problem of inaccurate bonding of sensors to sample surface.

The experimental investigations were supported by numerical simulations in a two-phase plane stress FE model, which reflects the contents of the real sample without taking into account the exact arrangement of particular aggregates. However, the limitations of this simplification were identified. The important issue was to identify the maximum frequency at which the method was efficient based on a comparison of the wavelength and aggregate size of the material. For frequencies above this limit, the real structure of the sample should be accurately reflected in the FE model due to diffraction of shorter waves at individual aggregates.

The efficacy of the procedure was proved by the similarity of the results obtained for samples made of the same material but with different sensor configurations. The initial results for both sensor configurations were different, however, the correction procedures determined by the training datasets led to similar final results.

As a first step in the development of more general attenuation-based diagnostic algorithm, the proposed method was used to analyse changes of the mass proportionality coefficient of concrete samples under the three-point bending test. The current results showed that attenuation changes can be potentially used as an indicator of fracture in concrete, however, further studies are needed to develop the efficient diagnostic method. The prospective applications include the detection of microcracks in concrete element under various loads, e.g., bending, compression or splitting. Further works will also incorporate the non-zero stiffness proportionality coefficient to verify its influence on the results.

CRediT authorship contribution statement

Erwin Wojtczak: Writing – original draft, Visualization, Software, Methodology, Investigation, Formal analysis, Conceptualization. **Magdalena Rucka:** Writing – review & editing, Supervision, Project administration, Methodology, Investigation, Funding acquisition, Conceptualization.

Declaration of competing interest

The authors declare the following financial interests/personal relationships which may be considered as potential competing interests: Magdalena Rucka reports financial support was provided by National Science Centre Poland. If there are other authors, they declare that they have no known competing financial interests or personal relationships that could have appeared to influence the work reported in this paper.

Acknowledgments

The study was financed by the National Science Centre, Poland, with project No. 2019/35/B/ST8/01905.

The corresponding author (EW) is supported by the Foundation for Polish Science (FNP).

Data availability

Data will be made available on request.

References

[1] T. Shiotani, S. Momoki, H. Chai, D.G. Aggelis, Elastic wave validation of large concrete structures repaired by means of cement grouting, Constr. Build. Mater. 23 (2009) 2647–2652, https://doi.org/10.1016/j.conbuildmat.2009.01.005.
[2] H. Choi, Y. Ham, J.S. Popovics, Integrated visualization for reinforced concrete using ultrasonic tomography and image-based 3-D reconstruction, Constr. Build. Mater. 123 (2016) 384–393, https://doi.org/10.1016/j.conbuildmat.2016.07.010.
[3] M. Zielińska, M. Rucka, Non-Destructive Assessment of Masonry Pillars using Ultrasonic Tomography, Materials (basel). 11 (2018) 2543, https://doi.org/10.3390/ma11122543.
[4] M. Słoński, K. Schabowicz, E. Krawczyk, Detection of flaws in concrete using ultrasonic tomography and convolutional neural networks, Materials (basel). 13 (2020) 1–16, https://doi.org/10.3390/ma13071557.
[5] G. Sha, H. Xu, M. Radzieński, M. Cao, W. Ostachowicz, Z. Su, Guided wavefield curvature imaging of invisible damage in composite structures, Mech. Syst. Sig. Process. 150 (2021), https://doi.org/10.1016/j.ymssp.2020.107240.
[6] E. Wojtczak, M. Rucka, Damage imaging algorithm for non-destructive inspection of CFRP/steel adhesive joints based on ultrasonic guided wave propagation, Compos. Struct. 297 (2022) 115930, https://doi.org/10.1016/j.compstruct.2022.115930.
[7] P.A. Gaydecki, F.M. Burdekin, W. Damaj, D.G. John, The propagation and attenuation of medium-frequency ultrasonic waves in concrete: A signal analytical approach, Meas. Sci. Technol. 3 (1992) 126–134, https://doi.org/10.1088/0957-0233/3/1/018.
[8] J.M. Berthelot, M. Ben Souda, J.L. Robert, Study of wave attenuation in concrete, J. Mater. Res. 8 (1993) 2344–2353, https://doi.org/10.1557/JMR.1993.2344.
[9] T.P. Philippidis, D.G. Aggelis, Experimental study of wave dispersion and attenuation in concrete, Ultrasonics 43 (2005) 584–595, https://doi.org/10.1016/j.ultras.2004.12.001.
[10] A. Abdullah, E.F. Sichani, Experimental study of attenuation coefficient of ultrasonic waves in concrete and plaster, Int. J. Adv. Manuf. Technol. 44 (2009) 421–427, https://doi.org/10.1007/s00170-008-1840-7.

[11] H.J. Yim, H.G. Kwak, J.H. Kim, Wave attenuation measurement technique for nondestructive evaluation of concrete, Nondestruct. Test. Eval. 27 (2012) 81–94, https://doi.org/10.1080/10589759.2011.606319.
[12] H. Sun, J. Zhu, Nondestructive evaluation of steel-concrete composite structure using high-frequency ultrasonic guided wave, Ultrasonics 103 (2020) 106096, https://doi.org/10.1016/j.ultras.2020.106096.
[13] L. Meirovitch, Fundamentals of vibrations, McGraw Hill Publications (2001).
[14] C. Ramadas, K. Balasubramaniam, A. Hood, M. Joshi, C.V. Krishnamurthy, Modelling of attenuation of lamb waves using rayleigh damping: Numerical and experimental studies, Compos. Struct. 93 (2011) 2020–2025, https://doi.org/10.1016/j.compstruct.2011.02.021.
[15] Z. Tian, L. Huo, W. Gao, H. Li, G. Song, Modeling of the attenuation of stress waves in concrete based on the Rayleigh damping model using time-reversal and PZT transducers, Smart Mater. Struct. 26 (2017), https://doi.org/10.1088/1361-665X/aa80c2.
[16] H. Mohseni, C.T. Ng, Rayleigh wave propagation and scattering characteristics at debondings in fibre-reinforced polymer-retrofitted concrete structures, Struct. Heal. Monit. 18 (2019) 303–317, https://doi.org/10.1177/1475921718754371.
[17] M. Treiber, J.Y. Kim, J. Qu, L.J. Jacobs, Effects of sand aggregate on ultrasonic attenuation in cement-based materials, Mater. Struct. Constr. 43 (2010) 1–11, https://doi.org/10.1617/s11527-010-9587-7.
[18] A. Sepehrinezhad, V. Toufigh, The evaluation of distributed damage in concrete based on sinusoidal modeling of the ultrasonic response, Ultrasonics 89 (2018) 195–205, https://doi.org/10.1016/j.ultras.2018.05.012.
[19] M. Ramaniraka, S. Rakotonarivo, C. Payan, V. Garnier, Effect of the Interfacial Transition Zone on ultrasonic wave attenuation and velocity in concrete, Cem. Concr. Res. 124 (2019) 105809, https://doi.org/10.1016/j.cemconres.2019.105809.
[20] T. Yu, J.F. Chaix, L. Audibert, D. Komatitsch, V. Garnier, J.M. Hénault, Simulations of ultrasonic wave propagation in concrete based on a two-dimensional numerical model validated analytically and experimentally, Ultrasonics 92 (2019) 21–34, https://doi.org/10.1016/j.ultras.2018.07.018.
[21] L. Lin, W. Zhang, Z. Ma, M. Lei, Porosity estimation of abradable seal coating with an optimized support vector regression model based on multi-scale ultrasonic attenuation coefficient, NDT E Int. 113 (2020) 102272, https://doi.org/10.1016/j.ndteint.2020.102272.
[22] J. Birdi, J. D'Hooge, A. Bertrand, A Neural Network Approach for Ultrasound Attenuation Coefficient Estimation, Eur. Signal Process. Conf. (2022) 902–906. https://doi.org/10.23919/eusipco55093.2022.9909948.
[23] P. Jarosik, M. Byra, M. Lewandowski, Z. Klimonda, Estimating the ultrasound attenuation coefficient using convolutional neural networks – a feasibility study, (2022). http://arxiv.org/abs/2205.09533.
[24] Y. Wang, C. Jin, L. Hu, W. Lu, A Deep Learning Normalization Method for Robust Ultrasound Attenuation Coefficient Estimation, Proc. - Int. Symp. Biomed. Imaging (2024) 1–5, https://doi.org/10.1109/ISBI56570.2024.10635392.
[25] S. El Hawwat, J. Kumar Shah, H. Wang, Machine learning supported ultrasonic testing for characterization of cracks in polyethylene pipes, Meas. J. Int. Meas. Confed. 240 (2025) 115609, https://doi.org/10.1016/j.measurement.2024.115609.
[26] S. Han, C. Li, Q. Han, X. Yao, Machine learning-aided prediction and customization on mechanical response and wave attenuation of multifunctional kiri/origami metamaterials, Extrem. Mech. Lett. 74 (2025) 102276, https://doi.org/10.1016/j.eml.2024.102276.
[27] A. Sciegaj, E. Wojtczak, M. Rucka, The effect of external load on ultrasonic wave attenuation in steel bars under bending stresses, Ultrasonics 124 (2022) 106748, https://doi.org/10.1016/j.ultras.2022.106748.
[28] T. Planès, E. Larose, A review of ultrasonic Coda Wave Interferometry in concrete, Cem. Concr. Res. 53 (2013) 248–255, https://doi.org/10.1016/j.cemconres.2013.07.009.
[29] E. Wojtczak, M. Rucka, Monitoring the curing process of epoxy adhesive using ultrasound and Lamb wave dispersion curves, Mech. Syst. Sig. Process. 151 (2021) 107397, https://doi.org/10.1016/j.ymssp.2020.107397.
[30] D. Alleyne, P. Cawley, A two-dimensional Fourier transform method for the measurement of propagating multimode signals, J. Acoust. Soc. Am. 89 (1991) 1159–1168, https://doi.org/10.1121/1.400530.
[31] F. Moser, L.J. Jacobs, J. Qu, Modeling elastic wave propagation in waveguides with the finite element method, NDT E Int. 32 (1999) 225–234, https://doi.org/10.1016/S0963-8695(98)00045-0.